NJC

ROYAL SOCIETY OF CHEMISTRY

PAPER

View Article Online
View Journal | View Issue

Check for updates

Cite this: *New J. Chem.*, 2020, 44, 5489

Reusable, few-layered-MoS_2 nanosheets/graphene hybrid on cellulose paper for superior adsorption of methylene blue dye†

Arthi Gopalakrishnan,‡[a] Satyam Pratap Singh‡[b] and Sushmee Badhulika ‡*[a]

Received 15th January 2020,
Accepted 10th March 2020

DOI: 10.1039/d0nj00246a

rsc.li/njc

In this study, we report for the first time few-layered MoS_2 nanosheets grown onto graphene dipped cellulose filter paper (M-G-CFP) using a simple hydrothermal method towards efficient adsorption of cationic methylene blue (MB) dye. Detailed morphological and chemical characterization studies of M-G-CFP are performed using FESEM, TEM, XRD and Raman spectroscopy that reveal micro flower-like MoS_2 grown onto graphene modified paper with few layers of MoS_2 nanosheets and its high purity nature. Due to electrostatic interactions between cationic dye and the anionic adsorbent surface, the hybrid M-G-CFP exhibits ultrafast removal of MB within 2 min with a maximum adsorption capacity of 485.4 mg g^{-1} which is superior in comparison to other reported MoS_2 based adsorbents. This high adsorption capacity is attributed to large accessible active sites on the surface of the hybrid M-G-CFP structure. The adsorption mechanism of MB dye on the MoS_2 nanosheets are well described using kinetic and isotherm models with the effects of parameters like pH, contact time and temperature. The kinetic and isotherm study reveals that the adsorption of MB dye follows a pseudo-second order model, indicating the chemisorption and Langmuir model of monolayer adsorption, respectively. Furthermore, this hybrid structure can be efficiently reused for subsequent dye adsorption without compromising on its dye removal efficiency suggesting it is a feasible and promising material towards wastewater treatment applications.

1. Introduction

Environmental deterioration due to industrialization has led to severe pollution across the globe. Industrial effluents from printing, textiles, leather, electroplating, and cosmetics, which includes organic dyes such as methylene blue, methyl orange, Rhodamine B, Azo dyes, *etc.*, have long term adverse health effects on human beings and are toxic to ecosystems.[1,2] Since these dyes are highly toxic and harmful, their removal from water is urgent and necessary. Numerous analytical approaches such as biological oxidation, photocatalysis, chemical oxidation and adsorption have been used to treat these dyes in wastewater effluents.[3] However, these techniques are expensive and are often unable to treat high concentrations of dye and other pollutants of water by photocatalysis and chemical oxidants, respectively.[4] Adsorption, on the other hand, is an economical and convenient approach that is widely applied for the efficient removal of organic dyes on a large scale. In addition, adsorption processes are simple, low cost, capable of treating diverse adsorbates, and demonstrate high efficiency for the removal of a high concentration of dyes.[5] Various adsorbents, such as activated carbons, clays, metal organic frameworks, composites and metal oxide materials have been developed to remove organic dyes and pollutants.[6–10]

Recently, two-dimensional nanomaterials have attracted considerable attention as potential materials for dye adsorption due to their unique properties like high surface area and large active sites that facilitate dye removal. Among them, MoS_2 has been widely explored due to its excellent electronic, photocatalytic, and optical properties.[11] MoS_2 is a 2D layered structure consisting of S–Mo–S *via* van der Waals forces with a high surface area that exhibits a strong absorption capacity and tunable band structure.[12,13] The main advantage of MoS_2 is its low cost and large-scale synthesis *via* a hydrothermal approach. Wang *et al.* reported flower-like MoS_2 as an adsorbent for Rhodamine B dye with the highest adsorption capacity of 49.2 mg g^{-1}.[14] Qiao *et al.* synthesized MoS_2 using a hydrothermal technique using polyethylene glycol as a surfactant

[a] *Department of Electrical Engineering, Indian Institute of Technology Hyderabad, Hyderabad 502285, India. E-mail: sbadh@iith.ac.in; Fax: +91-40-23016032; Tel: +91-40-23018443*

[b] *Department of Metallurgical and Materials Engineering, National Institute of Technology, Warangal, 506004, Telangana, India*

† Electronic supplementary information (ESI) available. See DOI: 10.1039/d0nj00246a

‡ Equally contributed to this manuscript.

towards the excellent removal of the MB dye.[15] On the other hand, graphene, yet another attractive 2D material, also has excellent electronic, thermal and mechanical properties and has been well reported towards the removal of heavy metal ions and dyes from aqueous solutions.[16,17] Thus, in addition to MoS_2, incorporating highly conductive 2D graphene nanosheets would provide enhanced properties resulting in high dye adsorption capacity. However, there are scarce reports on ultrafast adsorption of organic dyes based on MoS_2/graphene nanostructures optimized under different conditions like temperature, pH, *etc.*, along with a detailed study on the kinetics of adsorption.

In this study, we report the synthesis of a flower-like structure of ultrathin MoS_2 nanosheets grown onto graphene-coated cellulose filter paper (G-CFP) by simple hydrothermal process and its subsequent use for MB dye adsorption. Graphene dipped cellulose filter paper acts as a substrate for the growth of MoS_2 nanosheets and also provides excellent adsorption properties due to the capillary nature and porous property of the filter paper. The focus of the study is to investigate the effects of different process parameters namely pH, temperature and concentration of adsorbent on the adsorption ability of few-layered MoS_2 nanosheets of the MB dye. Furthermore, the adsorption mechanism and kinetic studies of MB dye are investigated in detail. More interestingly, this material can be reused for subsequent adsorption cycles without a major loss in adsorption capacity. Thus, the few-layered ultrathin MoS_2 nanosheets on G-CFP prepared with low cost and a scalable procedure exhibit excellent adsorption capacities with reusability that provides a sustainable solution for industrial wastewater treatment applications.

2. Experimental techniques

2.1. Chemicals and reagents

Whatman cellulose filter paper (CFP, grade 1) and graphene (Graphene supermarket, grade A-12) were purchased commercially. Sodium molybdate (Na_2MoO_4, $\geq$98%), thiourea (CH_4N_2S, 99%), and methylene blue (MB, >96%) were purchased from Sigma Aldrich. All reactions were done using deionized water (DI) from the Millipore system. Methylene blue aqueous solutions were prepared at different concentrations and were used for the adsorption experiments.

2.2. Synthesis of MoS_2 nanosheets on graphene-coated cellulose filter paper (M-G-CFP)

Schematic 1 illustrates the complete synthesis procedure of MoS_2 grown on cellulose filter paper. The cellulose filter paper (CFP) is soaked in a graphene solution (1 mg mL^{-1}) for 30 min and dried to obtain graphene-coated CFP (G-CFP). The G-CFP is then soaked in 10 ml seed solution containing 0.1 g of $Na_2MoO_4{\cdot}2H_2O$ and 0.2 g of CH_4N_2S for 1 h and dried at 80 °C. The as-obtained seeded substrate is then placed inside a Teflon-lined autoclave with a solution containing 0.3 g of $Na_2MoO_4{\cdot}2H_2O$ and 0.6 g of CH_4N_2S for the hydrothermal reaction at 200 °C for 24 h. The obtained product was washed with DI water and dried to receive few-layered ultrathin MoS_2 nanosheets on G-CFP denoted as M-G-CFP (Scheme 1).

2.3. Material characterization

The morphologies, microstructures, and number of MoS_2 nanosheet layers of samples were analyzed using a field emission scanning electron microscope (SEM, Oxford Instruments, 20 kV, Everhart-Thornley detector) and a transmission electron microscope (TEM, JEM-2100, 200 kV) with energy dispersive X-ray spectroscopy (EDS) by Zeiss, respectively. The crystal structure and thickness of the materials were determined by powder X-ray diffraction (XRD) obtained using a Bruker D advance XRD with Cu Kα radiation, 40 kV, 30 mA (λ = 1.54 Å) in the range of 2θ from 10° to 80° and Raman spectroscopy (WiTech instruments, 532 nm wavelength, 600 g mm^{-1}, 1800 nm spectral center) respectively. The surface area and pore analysis were measured by nitrogen sorption analysis using Micrometrics ASAP 2020 with a degassing temperature of 80 °C for 4 h. The pore size distribution was determined using Barrett–Joyner–Halenda (BJH) analysis. The optical properties of MoS_2 were analyzed using UV-vis spectroscopy provided by Shimadzu at a wavelength of 200–900 nm. The valence state of elements and its binding property was analyzed using X-ray photoelectron spectroscopy (Kratos Analytical, Axis Supra). The functional groups of the samples were analyzed using Fourier transform Infrared Spectroscopy (FTIR, Bruker spectrometer ALPHA II) from 400–4000 cm^{-1}. The surface charge of the sample was determined using Zeta potential measurements (Malvern panalytical Zetasizer Nano ZS90 at 30 °C, tracer measurement of 5).

2.4. Batch adsorption studies

Adsorption studies were performed using a 30 mL volume of MB solutions with initial concentrations from 100–300 mg L^{-1} in each beaker. The as-obtained M-G-CFP of equal mass (30 mg) was added to each 30 mL beaker containing MB solution and kept under stirring for 24 h to reach equilibrium conditions. To analyze the effect of parameters like pH and temperature,

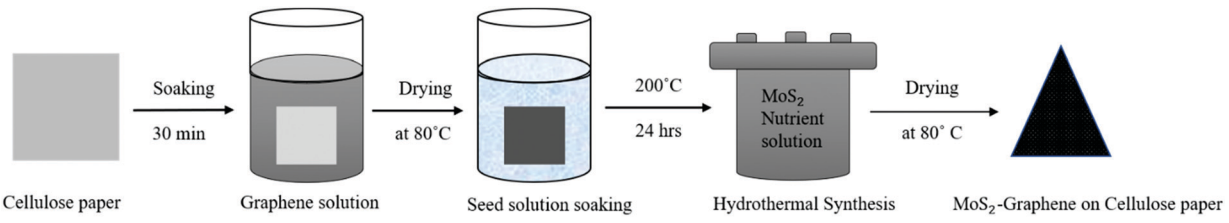

Scheme 1 Synthesis process of ultrathin MoS_2 nanosheets/graphene on cellulose filter paper (M-G-CFP) using a hydrothermal technique.

the initial concentration of MB with 30 mg of M-G-CFP adsorbent was kept in pH 1 to 13 and 30–70 °C, respectively and were analyzed after 30 min of the adsorption process. All the samples were centrifuged prior to analysis to reduce the interference of the M-G-CFP spectrum with the MB dye. The concentration of MB from each experiment before and after adsorption was analyzed using a UV-Vis spectrophotometer (Shimadzu) at 664 nm. The amount of MB adsorption at equilibrium, Q_e (mg g^{-1}), and its percentage removal efficiency was calculated using the formulae given by:

$$Q_e = \frac{(C_0 - C_e)V}{W} \quad (1)$$

$$\%\text{Removal} = \frac{C_0 - C_e}{C_0} \times 100 \quad (2)$$

where C_0 and C_e (mg l^{-1}) are initial and equilibrium concentrations of MB, respectively. V is the volume of the solution (l) and W is the mass of adsorbent (g).

3. Results and discussion

The formation of few-layered ultrathin MoS_2 nanosheets was successfully achieved using a simple hydrothermal process using G-CFP as a substrate, as depicted in Scheme 2. The graphene-coated CFP due to its rough surface provides high energy sites for nucleation and facilitates the growth of flower-like MoS_2 assembled ultrathin nanosheets. The uniformly grown few-layered MoS_2 nanosheet arrays on G-CFP were further subjected to investigations of MB dye adsorption.

3.1. Characterization of M-G-CFP material

The morphology of the few-layered MoS_2 grown onto G-CFP is displayed in Fig. 1(a), exhibiting both low and high magnification images (inset) with a uniform coating of MoS_2 nanosheet arrays. The inset of Fig. 1(a) shows a growth of ultrathin MoS_2 nanosheets aligned to form micro flower structures and each micro flower structure consists of individual ultra-thin MoS_2 nanosheets interconnected together. From the high-resolution image in Fig. 1(b), the ultrathin layer nanosheet arrays are visible clearly with thicknesses ranging approximately from 50–100 nm. The elemental composition was analyzed using EDS and its corresponding spectrum is given in Fig. 1(c), which indicates the absence of impurities. The percentage of each element is tabulated in Fig. 1(d) where the carbon percentage indicates the presence of graphene nanosheets. Fig. 1(e) and (f) display low and high magnification TEM images, respectively, where the ultrathin MoS_2 nanosheets are clearly visible. The high-resolution TEM image in Fig. 1(d) exhibits a lattice spacing of 0.62 nm which corresponds to the (002) plane of MoS_2 and indicates the formation of 3–8 layered nanosheets.[18]

The crystal phases of M-G-CFP were analyzed by XRD, and the results are given in Fig. 2(a). The spectrum shows sharp peaks at 26.2° and 54.8° indexed to the (002) and (004) planes of graphite, respectively, which indicates the presence of a multilayer structure of graphene.[19] The enlarged XRD spectra given in the inset exhibits clear peaks of pure crystalline MoS_2 nanosheets grown on G-CFP with the existence of a 2H phase along with strong graphene peaks. The diffraction peaks at 13.5°, 32.6°, 39.2°, 43.3°, and 57.2° correspond to the (002), (100), (103), (006) and (110) planes, respectively (JCPDS card no. 37-1492), without any impurity confirming the high purity crystalline phases of the MoS_2 nanosheets.[20] The XRD pattern of graphene-coated CFP is given in Fig. S1(a) (ESI†), where it exhibits the characteristic peaks of (002), (100) and (004) corresponding to graphene layers. The interlayer spacing of 6.2 Å of the (002) plane matches well with the lattice spacing given in the high-resolution TEM image.

To determine the thickness of the MoS_2 nanosheets, Raman spectroscopy analysis was studied as depicted in Fig. 2(b). The two main Raman active modes of A_{1g} and E_{2g} located at 407 cm^{-1} and 377 cm^{-1} correspond to the out-of-plane vibration of sulfides. The large discrepancy between these two modes of vibration indicates relatively few MoS_2 layers (4–5 layers), in accordance with the HRTEM lattice spacing.[21] This suggests that few-layered MoS_2 nanosheets with large active sites along with graphene-coated CFP benefits MB adsorption. In continuation with the higher Raman shift, significant peaks of graphene at 1340 cm^{-1} and 1570 cm^{-1} are formed, which correspond to the defective D band and graphitic G band, respectively. The characteristic peak at 2685 cm^{-1} indicates the second-order band of graphene and its less intensity compared to G band exhibits the stacked multilayer graphene nanosheets.

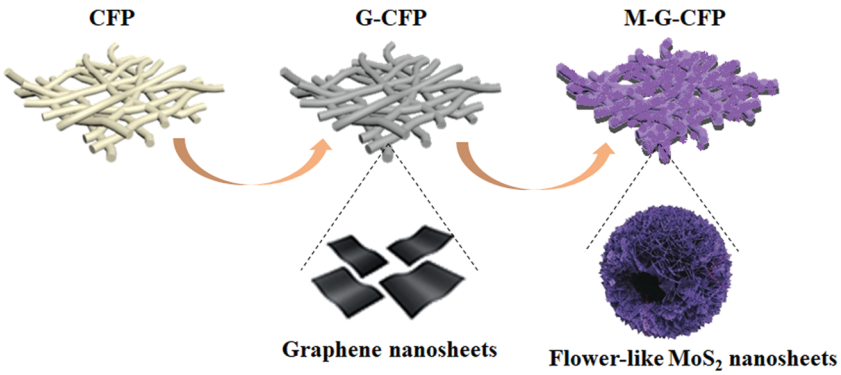

Scheme 2 Hydrothermal synthesis of ultrathin MoS_2 nanosheets/graphene on cellulose filter paper (M-G-CFP).

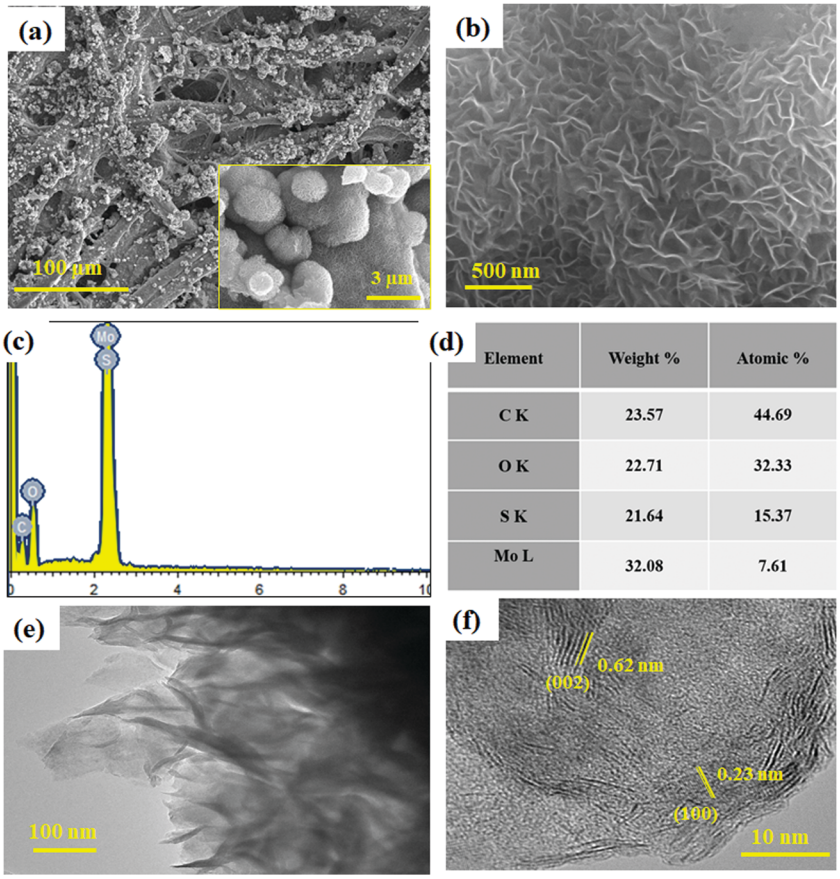

Element	Weight %	Atomic %
C K	23.57	44.69
O K	22.71	32.33
S K	21.64	15.37
Mo L	32.08	7.61

Fig. 1 (a) Low & (b) high magnification FESEM images; (c) EDS spectrum; (d) elemental composition; (e) TEM image and (f) high-resolution TEM image of ultrathin MoS_2 nanosheets/graphene on cellulose filter paper (M-G-CFP).

The Raman spectrum of pure graphene-coated CFP without MoS_2 is shown in Fig. S1(b) (ESI†). The optical properties of the as-obtained M-G-CFP were investigated using UV-Vis spectroscopy, as displayed in Fig. S2 (ESI†), to determine the bandgap and its phase formation. The spectrum shows an absorption peak at 250–300 nm with an increase in the UV region from 600–800 nm. The bandgap of the MoS_2 was estimated from the Tauc plot of $(\alpha h\nu)^2$ *versus* $h\nu$ given in Fig. S2 (ESI†) (inset) by extrapolating a straight line to the X-axis intercept, indicating a bandgap of 1.9 eV.

Furthermore, the hybrid structure of M-G-CFP exhibits a good surface area with type IVa isotherm curve and H2(b) hysteresis loop given in Fig. S3(a) (ESI†). This N_2 adsorption/desorption isotherm curve indicates the mesoporous capillary condensation adsorption nature with the pore width exceeding the critical width. The type of hysteresis loop is associated with the percolation in the narrow range with larger widths.[22] After the adsorption of the MB dye, the surface area (4.3 $m^2\ g^{-1}$) decreases rapidly compared to the surface area before adsorption (34.9 $m^2\ g^{-1}$). Fig. S2(b) (ESI†) shows the pore size distribution curve which exhibits pore sizes ranging from meso to macro pores. However, after adsorption of MB dye molecules, the pore volume decreases due to the adsorption process onto the surface of the adsorbent. These properties of the hybrid structure, such as large active surface sites, accessible porous natures and interconnected structure enhance the adsorption property of pollutants onto its surface.

The chemical features and bonding states of M-G-CFP were examined by XPS, and the results are shown in Fig. 2(c–g). The wide scan survey spectrum in Fig. 2(c) displays the peaks of Mo, S from MoS_2 and C, O from graphene on CFP. The deconvoluted Gaussian fitting of Mo 3d, exhibits two characteristic doublet peaks at 229.2 eV ($3d_{5/2}$) and 232.5 eV ($3d_{3/2}$) corresponding to the 4+ oxidation state of MoS_2. The lower and higher energy shoulder peaks detected at 226.4 eV and 235.7 eV, are ascribed to the S 2s state and Mo 6+ oxidation state, respectively. Fig. 2(d) exhibits the S 2p spectra deconvoluted to two peaks at 161.9 eV ($2p_{3/2}$) and 163.1 eV ($2p_{1/2}$) corresponding to the divalent sulfide ions in MoS_2.[23] These divalent ions cause the anionic surface charge that serves as the electrostatic adsorption point for the cationic MB dye molecules. The C 1s spectrum in Fig. 2(e) shows two main peaks at 284.4 eV and 288.2 eV corresponding to sp^3 and sp^2 bonds, respectively. The O 1s spectrum displays two peaks at 529.4 eV and 531.2 eV ascribed to the O2- and OH-bonding state, respectively. The broad peak at 531.2 eV implies the presence of more defects on the surface of the M-G-CFP material, which enhances the interfaces for the adsorption.

3.2. Effect of contact time

The maximum adsorption of MB on the surface of the adsorbent can be determined by the contact time that designates the

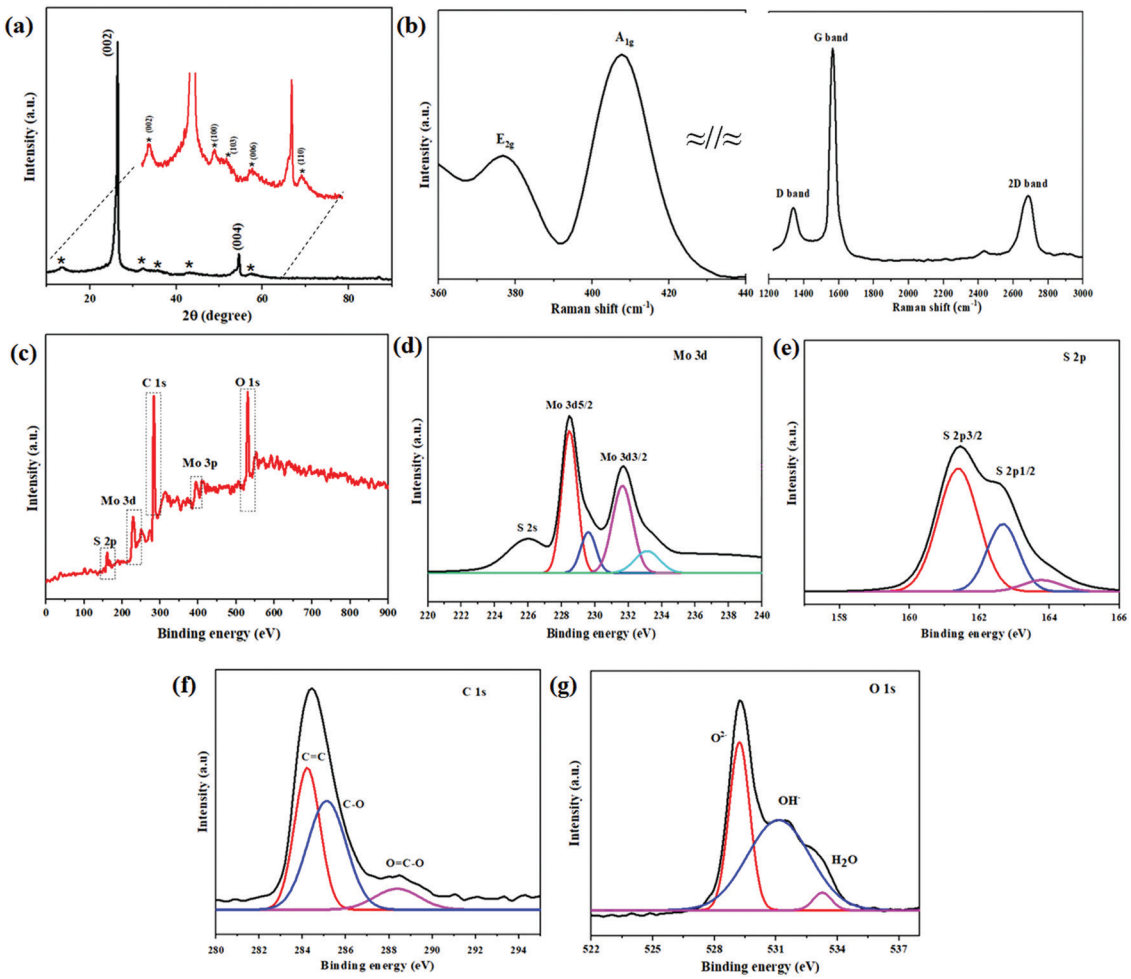

Fig. 2 Analysis of ultrathin MoS_2 nanosheets/graphene on cellulose filter paper (M-G-CFP) using (a) XRD spectrum; (b) Raman spectrum; (c) XPS survey spectrum; high-resolution spectrum of (d) Mo 3d; (e) S 2p; (f) C 1s and (g) O 1s.

maximum adsorption at a suitable time of contact. Fig. 3 illustrates the effect of the contact time (0–400 s) of MB adsorption on M-G-CFP for different concentrations of MB solution. It is observed that there is a sharp increase in the initial 10 s of adsorption and after 10 s there is a slight increment in the adsorption capacity. This result states that during the primary adsorption process, all the vacant sites on the M-G-CFP surface were readily available for the rapid adsorption of MB dye molecules.[24] As adsorption progresses the available number of surface vacant sites reduces, and repulsion occurs between the adsorbent and adsorbate molecules.[25] At last, the equilibrium stage is attained wherein the adsorption/desorption rates are identical and an increase in adsorption capacity is no longer observed. This suggests that M-G-CFP can act as an efficient and ultrafast adsorbent for organic dye removal.

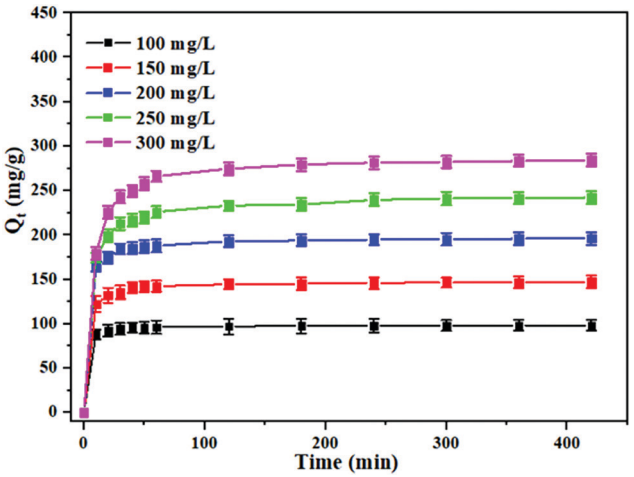

Fig. 3 Effect of contact time of MoS_2 nanosheets/graphene on cellulose filter paper (M-G-CFP) on MB dye adsorption under various concentrations of MB (100–300 mg L^{-1}; 298 K; pH 7).

3.3. Adsorption kinetics

To determine the plausible adsorption mechanism and interpret the adsorption process, the most used kinetic models such as pseudo-first-order and second-order models were acquired for investigating MB dye adsorption behavior on the surface of M-G-CFP adsorbent. The non-linear curve fitting from the original kinetics equation was also adopted to avoid the

plausible errors and acquire the best fitting equation. The pseudo-first-order model is based on the speculation that the rate of adsorption is directly proportional to the number of adsorption active sites of the adsorbent given by the following equation by Langergren and Svenska:

$$\text{Non-linear: } Q_t = Q_e(1 - e^{-K_1 t}) \quad (3)$$

$$\text{Linear: } \ln(Q_e - Q_t) = \ln Q_e - K_1 t \quad (4)$$

where Q_e and Q_t are the concentration of adsorbed (mg g^{-1}) MB at equilibrium and at time t (min), respectively, and K_1 is the rate constant of pseudo-first-order kinetics (min^{-1}).

The pseudo-second-order model based on equilibrium adsorption is expressed by the following equation:

$$\text{Non-linear: } Q_t = \frac{K_2 Q_e^2 t}{1 + K_2 Q_e^2 t} \quad (5)$$

$$\text{Linear: } \frac{t}{Q_t} = \frac{1}{K_2 Q_e^2} + \frac{1}{Q_e} t \quad (6)$$

where K_2 is the pseudo-second-order rate constant (g mg^{-1} min^{-1}).

Fig. 4(a) represents a pseudo-first-order model of MB adsorption on M-G-CFP under different concentrations of MB solution. The linear regression (R^2) values obtained from the plot were found to be in the range of 0.82 to 0.95 (low value), indicating a poorly fitted linear plot. Moreover, the calculated Q_e values did not match with the experimental (Q_e) values at each different concentration of adsorbent. This behavior indicates that the pseudo-first-order model cannot determine the adsorption kinetics process. However, the pseudo-second-order model has a perfect linear fit of $\frac{t}{Q_t}$ *versus* t, which is given in Fig. 4(b) with R^2 values in the 0.999–1 range higher than the pseudo-first-order kinetics. Also, the calculated Q_e values were nearly equal to the experimental Q_e values, which reveals that the adsorption kinetics is well-fitted and the adsorption process of MB onto the M-G-CFP adsorbent follows the pseudo-second-order kinetics model. The calculated Q_e values of adsorption models are given in Table 1.

The third kinetic model called intra-particle diffusion was also analyzed to investigate the plausible diffusion of MB into adsorbent pores by the following equation:

$$Q_t = K_{diff}\sqrt{t} + C \quad (7)$$

where K_{diff} is the intraparticle diffusion rate constant (mg g^{-1} $min^{-1})^{1/2}$, $\sqrt{t}$ is the square root of time, and C is a constant that provides information about the thickness of the boundary layer.

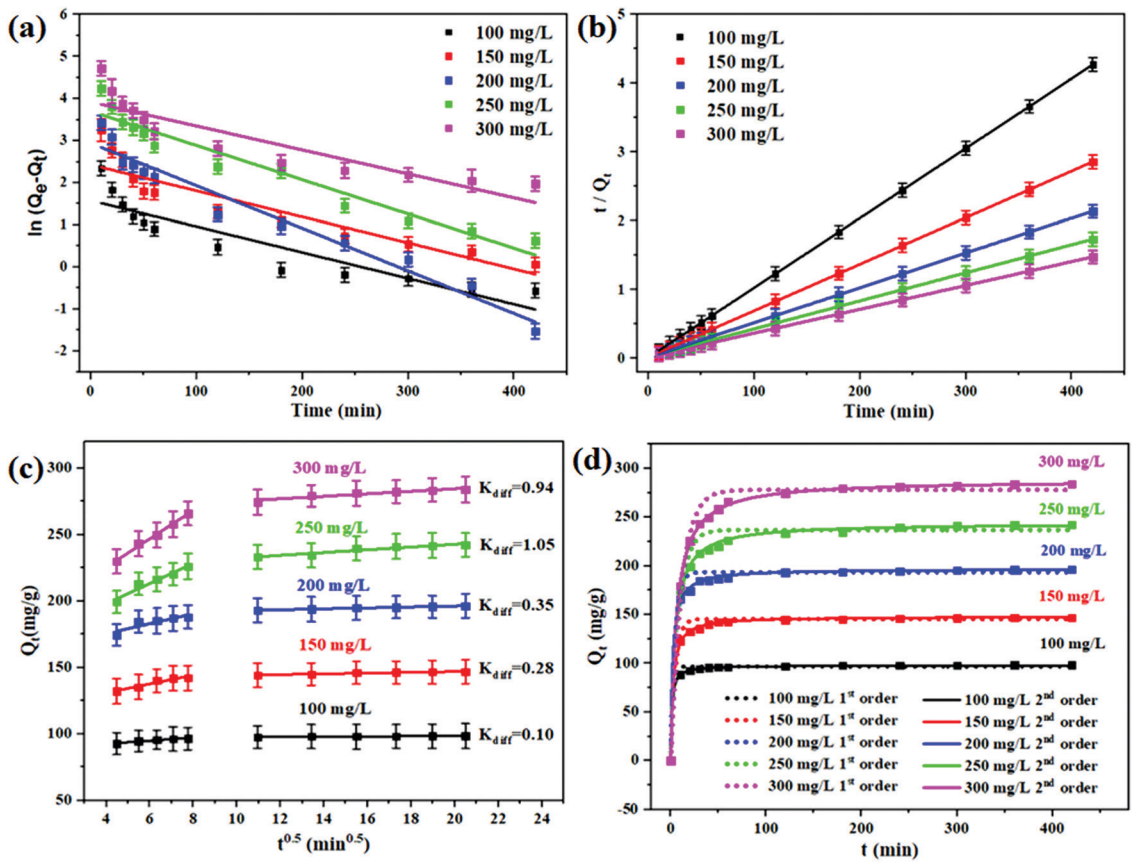

Fig. 4 Linear regression (a) pseudo-first-order kinetics; (b) pseudo-second-order kinetics; (c) intraparticle diffusion and (d) non-linear regression kinetics of pseudo-first order and second-order models for MB adsorption (100–300 mg L^{-1}; 298 K; pH 7, 30 mg dosage) on MoS_2 nanosheets/graphene on cellulose filter paper (M-G-CFP) adsorbent.

Table 1 Linear and non-linear kinetic parameters of MB adsorption onto ultrathin MoS_2 nanosheets/graphene on cellulose filter paper (M-G-CFP) at 298 K (30 mg dosage at pH 7)

		Concentration of MB dye				
Model	Para	100 mg L^{-1}	150 mg L^{-1}	200 mg L^{-1}	250 mg L^{-1}	300 mg L^{-1}
Pseudo-first order	R^2	0.83	0.86	0.95	0.94	0.82
Pseudo-first order (non-linear)	R^2	0.90	0.90	0.90	0.91	0.92
Pseudo-second order	R^2	1	0.99	0.99	0.99	1
	K_2	0.0076	0.0028	0.0019	0.0007	0.0006
	$Q_{e,cal}$	98.62	147.71	197.23	245.09	288.18
	$Q_{e,Exp}$	98.85	148.06	196.5	244.17	291.18
Pseudo-second order (non-linear)	R^2	0.99	0.99	0.99	0.99	0.99
	K_2	0.0093	0.0029	0.0023	0.0009	0.0006
	$Q_{e,cal}$	98	148	197	244	288
	$Q_{e,Exp}$	98.85	148.06	196.5	244.17	291.18
Intra-particle diffusion	R^2	0.77	0.73	0.77	0.84	0.81
	K_{diff}	0.28	0.72	1.03	2.26	2.90

Fig. 4(c) shows the plot between Q_t *vs.* $t^{1/2}$, from which the intraparticle diffusion rate constant K_{diff} is obtained from the slope of the straight line. The intraparticle diffusion gave lesser R^2 values (0.77–0.84) compared to the first-order model. Also, the line does not pass through the origin, which suggests that intraparticle diffusion kinetics is not the rate-controlling step of the adsorption process. The non-linear regression kinetics of pseudo-first order and pseudo-second order models are plotted against Q_t *vs.* t, as shown in Fig. 4(d). Likewise, linear regression, the non-linear fit of pseudo-second-order kinetics were well-fitted with regression (R^2) values of 0.99. Thus, according to the pseudo-second-order assumption, the adsorption of MB is based on chemisorption as the rate-controlling step which involves the exchange or sharing of electrons between the cationic MB dye and anionic adsorption sites of M-G-CFP by valence forces.[26]

3.4. Adsorption isotherms

To evaluate the adsorption capacity and the interaction of adsorbates with adsorbents, the adsorption isotherms were investigated. These isotherms indicate the distribution of adsorbate molecules between the solid and liquid phase at equilibrium adsorption states. The two most common isotherms of Langmuir and Freundlich isotherms were analyzed by both linear and non-linear regression fitting. The adsorption isotherm and its parameters for the control samples of cellulose filter paper and graphene coated cellulose filter paper were also analyzed and are given in Fig. S3 and Table S1 (ESI†), respectively. Compared with the control samples, the M-G-CFP composite was found to have a high adsorption ability due to the synergistic effect between the materials.

Langmuir isotherm. The assumption states that the monolayer adsorption with uniform strategies on the surface of the adsorbate containing active adsorption sites without any *trans*-migration of the adsorbate.[27] The linear and non-linear regression equation of the Langmuir isotherm are given as:

$$\text{Non-linear: } Q_e = \frac{Q_0 b C_e}{1 + bC_e} \tag{8}$$

$$\text{Linear: } \frac{C_e}{Q_e} = \frac{1}{Q_0 b} + \frac{1}{Q_0} C_e \tag{9}$$

where C_e is the equilibrium concentration of the adsorbate (mg L^{-1}), Q_0 and b are the constants of adsorption capacity and rate of adsorption, respectively. The plot of $\frac{C_e}{q_e}$ *versus* C_e is shown in Fig. 5(a) with slope $\frac{1}{Q_0}$. The regression coefficient value (R^2) of 0.996 indicates that the MB adsorption onto the M-G-CFP adsorbent was well-fitted to the Langmuir isotherm model. The maximum adsorption capacity was found to be 401.6 mg g^{-1} and the rate of adsorption was 0.286 l mg^{-1}. The non-linear regression plot against Q_e *vs.* C_e is shown in Fig. 5(c), from which the maximum adsorption capacity was found to be 485.4 mg g^{-1} with a rate of adsorption of 0.239 l mg^{-1}.

The essential characteristics of the Langmuir isotherm were determined using an equilibrium parameter R_L, by the following equation:

$$R_L = \frac{1}{1 + bC_0} \tag{10}$$

where R_L determines the condition of the isotherm reaction, if $R_L = 0$, the isotherm is irreversible; if $R_L = 1$, the isotherm is linear; if $R_L > 1$, the isotherm is unfavorable; and if $0 < R_L < 1$, the isotherm is favorable. The R_L values obtained were 0.0069 (linear) and 0.0137 (non-linear) at 25 °C, which lies between $0 < R_L < 1$ indicating that the Langmuir isotherm is favorable towards the adsorption process of MB onto the M-G-CFP adsorbent.

Freundlich isotherm. On the other hand, the Freundlich isotherm states that adsorption takes places through heterogeneous surface energies, in which the energy term in the Langmuir equation varies as a function of surface coverage given by the following equation:[28]

$$\text{Non-linear: } Q_e = K_f C_e^{\frac{1}{n}} \tag{11}$$

$$\text{Linear: } \log Q_e = \log K_F + \left(\frac{1}{n}\right) \log C_e \tag{12}$$

where K_F and n are Freundlich constants corresponding to the adsorption capacity of the adsorbent for a unit equilibrium concentration and an indication of favorable condition of the

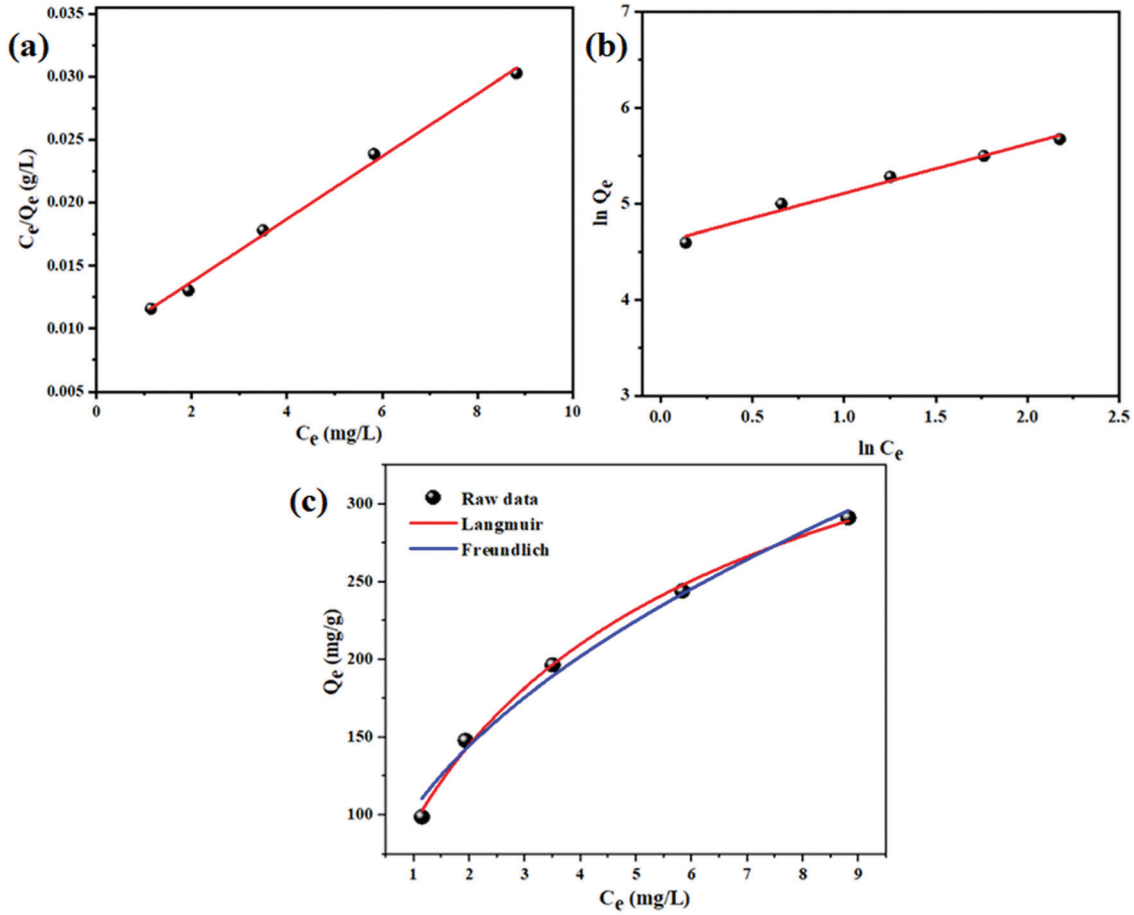

Fig. 5 (a) Langmuir and (b) Freundlich linear isotherms and (c) the non-linear regression isotherm of MB adsorption on the MoS_2 nanosheets/graphene on cellulose filter paper (M-G-CFP) adsorbent (100–300 mg L^{-1}; 298 K; pH 7, 30 mg dosage).

adsorption process, respectively. The value of the slope gives the measure of surface heterogeneity or adsorption intensity, where the value below one represents a normal Langmuir isotherm and the above one indicates cooperative adsorption. The linear regression plot shown in Fig. 5(b) with $\log Q_e$ *versus* $\log C_e$ represents a straight line with a slope of $1/n$ = 0.51, thus confirming a normal Langmuir isotherm. The non-linear regression curve from Fig. 5(c), shows the fitting with a slope of $1/n$ = 0.481, further confirming the Langmuir isotherm behavior. The values of adsorption isotherm parameters are given in Table 2.

3.5. Effect of pH

The pH of the solution plays a key role in the adsorption process since it affects the surface charge of the adsorbents and ionization of the adsorbate molecules. The effect of pH on adsorption equilibrium after 30 min is given in Fig. 6(a) with an initial concentration of MB (100 mg L^{-1}). It depicts that the adsorption of MB dye increases as the pH of the solution increases with a consistent trend which in turn states that M-G-CFP adsorbs a high amount of MB dye at the higher alkaline solution. The adsorption increased rapidly until pH 5 and equilibrium is noted from pH 7 to 13 with an average of 98.65 mg g^{-1}. The lowest adsorption equilibrium of 53.32 mg g^{-1} was obtained at pH 1. Thus, optimum pH for MB adsorption on M-G-CFP adsorbent is 7 and it explains the electrostatic interaction between the surface of the negatively charged adsorbent with the MB cationic dye. This is in agreement with the report which states that MoS_2 nanosheets above

Table 2 Linear and non-linear isotherm parameters for MB adsorption on ultrathin MoS_2 nanosheets/graphene on cellulose filter paper (M-G-CFP) adsorbent (30 mg dosage at pH 7)

Isotherms	Parameters	Temperature at 298 K
Langmuir (linear)	Q_0 (mg g^{-1})	401.6
	b (L mg^{-1})	0.2845
	R_L	0.0069
	R^2	0.99
Langmuir (non-linear)	Q_0 (mg g^{-1})	485.4
	b (L mg^{-1})	0.2397
	R_L	0.0137
	R^2	0.99
Freundlich (linear)	K_f ($mg^{1-1/n}$ $L^{1/n}$ g^{-1})	98.7
	$1/n$	0.5149
	R^2	0.98
Freundlich (non-linear)	K_f ($mg^{1-1/n}$ $L^{1/n}$ g^{-1})	97.7
	$1/n$	0.481
	R^2	0.98

pH 3, have a negative surface charge, and its zeta potential increases in the direction of alkaline pH indicating its effective adsorption of positively charged MB dye.[29]

3.6. Effect of temperature

Temperature is the main parameter to be considered during the adsorption process of dyes since it affects the rate of adsorption and solution viscosity which in turn affects the adsorption capacity at equilibrium. Fig. 6(b) illustrates the plot of adsorption equilibrium as a function of temperature at the end of 30 min of MB adsorption. For the initial concentration of MB (100 mg L^{-1}), the adsorption equilibrium increases with an increase in temperature and reached a maximum at 318 K with an adsorption equilibrium of 99.85 mg g^{-1} indicating the endothermic nature of the adsorption reaction. With a further increase in temperature, there is a decrease in adsorption equilibrium which is possibly due to the lesser number of adsorption sites and no occurrence of intraparticle diffusion of dye molecules.[26]

3.7. Effect of presence of salt ions

The effect of the presence of ions like Na^+, SO_4^{2-}, and Ca^{2+} at different molar concentrations on MB (100 mg L^{-1}) adsorption by M-G-CFP is given in Fig. 6(c). It is clear that the presence of monovalent and divalent ions during adsorption of MB dye hinders the adsorption quantity of the adsorbate.[30] The adsorption equilibrium values for M-G-CFP in the presence of ions follow the order: without salt < SO_4^{2-} < Na^+ < Ca^{2+}. The adsorption equilibrium of MB in the presence of 0.1 M Na_2SO_4, NaCl and $CaCl_2$ are 84.32, 79.63 and 76.38 mg g^{-1}, respectively. The MB dye molecules are adsorbed onto negatively charged ions like Cl^- and SO_4^{2-} mainly due to electrostatic interaction and that causes a repulsive force on the adsorbent by decreasing the adsorption efficiency. The presence of cations like Na^+ and Ca^{2+} pairs to the anionic surface of M-G-CFP by the electrical double layer formation. The divalent cation (Ca^{2+}) has a much higher effect than monovalent cation (Na^+) on the adsorption of MB at the adsorbent–adsorbate interface. Thus, the anions impart a repulsive effect on the adsorbent resulting in less effect on adsorption equilibrium compared to the presence of cations, that directly binds to the adsorbent.

3.8. Reusability test

The ideal efficiency of the adsorbent is determined by assessing its reusability, which greatly reduces the cost. The reusability study was evaluated by MB adsorption efficiency (%) on M-G-CFP for four consecutive cycles as given in Fig. 6(d). The initial dye concentration of 100 mg L^{-1} with 50 mg of adsorbent loading

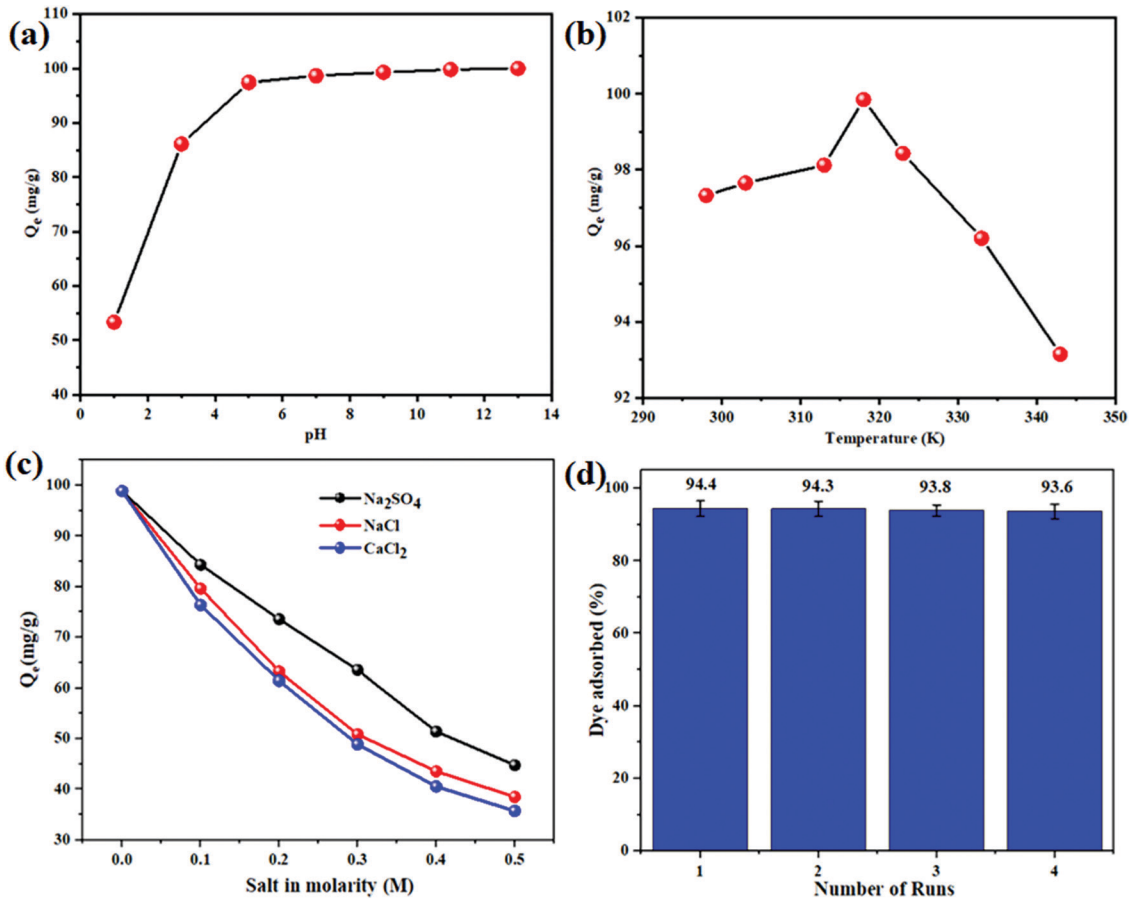

Fig. 6 (a) Effect of pH; (b) effect of temperature; (c) effect of the presence of salt ions; and (d) reusability of ultrathin MoS_2 nanosheets/graphene on cellulose filter paper (M-G-CFP) adsorbent on MB dye (100 mg L^{-1}, 298 K, pH 7 for 30 mg of dosage).

to 50 ml of dye solution was used for the reusability tests. After the dye adsorption process, the solution was centrifuged to separate the adsorbent. The adsorbent was washed in 0.5 M HCl acidic solution (pH of ~2) by sonication followed by DI water. It was then dried at 100 °C and reused for the next cycle of MB adsorption. The initial adsorption efficiency of MB was 94.4% on the surface of the adsorbent which showed a slight decrement at the end of the 4th cycle with 93.6% efficiency. This explains its excellent reusability for adsorbing the dye without any significant degradation on efficiency and adsorption sites.

3.9. FT-IR spectrum and zeta potential analysis

To further study the mechanism of MB adsorption on M-G-CFP, the FT-IR spectrum comparison of M-G-CFP before and after MB adsorption was obtained as shown in Fig. 7(a). The initial concentration of MB dye (100 mg ml^{-1}) was required for adsorption and to attain equilibrium, which was dried to obtain M-G-CFP with MB dye. The FT-IR spectrum of M-G-CFP before MB adsorption has strong characteristic peaks at 3427, 908, and 590 cm^{-1} indicating the presence of –OH, Mo═O and –SH bonds, respectively.[31] The significant peaks at 1630, 1400 and 1054 cm^{-1} are ascribed to the C═C, C–OH, and C–O–C vibration respectively, indicating the carbon bond stretching in graphene. After MB dye adsorption on M-G-CFP, the position of the characteristic peak of the d–OH bond shifted to higher frequencies from 3427 to 3457 cm^{-1}. In addition, the strong characteristic peaks of –C–OH, C═C and –SH bonds became weak. These changes in the characteristic bands before and after MB adsorption indicate that the mechanism of adsorption on M-G-CFP are distributed on the surface *via* hydrogen bonds. The new peaks at 1397, 1330, 1037, and 877 cm^{-1} correspond to the ═C–N, –C–N, –C–S and ═C–H bonds of MB dye which are not visible in the pristine M-G-CFP sample before adsorption.

The surface charge of the adsorbent and its absorption behavior towards cationic dye was carried out using zeta-potential measurements. Fig. 7(b) shows that M-G-CFP has a negative surface charge and the zeta-potential increases to a more negative charge as the pH increases towards alkaline, indicating that the adsorbent has abundant acidic sites for dye adsorption.[31] The negative surface charge is due to the functional groups (–OH and –COOH) attached, evident from the FT-IR spectrum. Hence, the electrostatic attraction between the anionic surface of the adsorbent and cationic dye is the main factor for adsorption for MB dye.

In addition, the settling rate of the adsorbent determines the faster retrieval/removal of the adsorbent from contaminated dye solution. The as-synthesized M-G-CFP exhibited a faster settling rate which is useful in retrieving the adsorbent by simple processing and making it beneficial for economical use. To study its settlement rate, 1 g of adsorbent was mixed in 500 ml water at 25 °C and stirred at 300 rpm for 30 min to disperse it homogeneously and later it was allowed to settle down completely. The water level measured was 5.1 cm and the adsorbent material settled completely in 62 seconds. The settling rate was found to be 0.822 mm per second which is calculated using water level height and time taken to settle down.

There are very few reports on the usage of two-dimensional MoS_2 nanosheet based adsorbents for organic dyes as given in Table 3. Massey *et al.* reported MoS_2 nanosheets for MB dye adsorption which had 297 mg g^{-1} maximum adsorption capacity.[34] Though it has large active sites for adsorption, the capacity of adsorption is less due to the absence of a porous nature. Fang *et al.*, synthesized MoS_2-glue sponges for the efficient removal of Rhodamine B dye with a maximum adsorption capacity of 127.39 mg g^{-1} in 60 min.[35] Also, reports on magnetic nanocomposites with MoS_2 were prepared and successfully applied in the removal of dyes using an external magnetic field.[36,37] These reported works on MoS_2 nanosheets reveal that it requires a longer adsorption time with low adsorption capacity. Therefore, it indicates that further enhancement in adsorption capacity, rate of adsorption and reusability is of prime significance. In this study, we have prepared ultrathin few-layered MoS_2 nanosheets grown onto graphene-modified cellulose filter paper as a framework containing the porous nature which enhances the active sites due to its high surface area for adsorption. Thus, the high adsorption capacity of

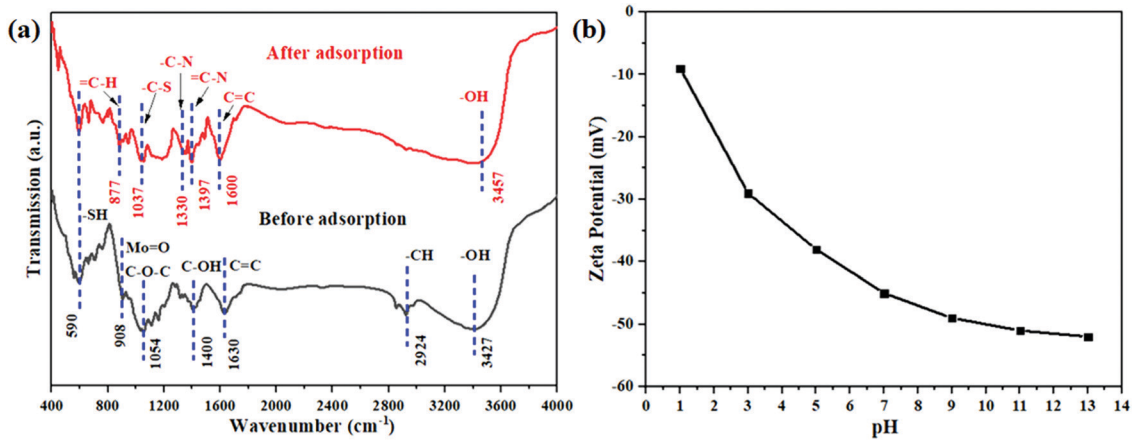

Fig. 7 (a) FT-IR spectrum of M-G-CFP before and after adsorption of MB dye (100 mg L^{-1}; 298 K; pH 7 with 30 mg of dosage after 30 min); (b) zeta-potential of M-G-CFP at different pH solutions.

Table 3 Comparison of organic dye adsorption capacity of MoS_2 based reports with MoS_2/graphene hybrid on cellulose paper (M-G-CFP):

Adsorbent	Dye	Maximum dye adsorption (Q_{max}) in mg g^{-1}	Ref.
MoS_2–polymer composite	Methylene blue	244.03	32
MoS_2 nanostructure	Methylene blue	208	29
N-Doped MoS_2 nanocrystals	Methylene orange	134.89	33
MoS_2 nanosheets	Methylene blue	297	34
Cellulose/graphene oxide	Methylene blue	480.7	38
MoS_2 microspheres	Methyl orange	38.11	39
Activated carbon rom finger citron residue	Methylene blue	581.4	6
Zn/Cu—BTC@MC composite	Congo red	1078	8
MoS_2/graphene on cellulose filter paper (M-G-CFP)	**Methylene blue**	**485.4**	**This work**

485.4 mg g^{-1} is achieved and is reusable for subsequent dye removal processes with high removal efficiency making it attractive for wastewater treatment applications.

4. Conclusion

In summary, facile hydrothermal synthesis of ultrathin few-layered MoS_2 nanosheets as micro flowers on a graphene-coated cellulose paper is reported for high capacity MB dye adsorption. TEM images reveal that each micro flower consists of ultrathin nanosheets of MoS_2 arranged as petal structures with 50–100 nm width. The adsorption rate of MB dye onto M-G-CFP adsorbent was ultrafast and exhibits an impressive adsorption capacity due to its electrostatic interaction between cationic MB dye and anionic adsorbent surface. The adsorption behavior of M-G-CFP is well fitted with the Langmuir isotherm and pseudo-second-order kinetic model. The batch experiments with the effect of parameters like pH, temperature and contact time on the adsorbent were optimized for the concentration of the MB dye adsorption. Importantly, the adsorbent can be reused subsequently without any significant drop in adsorption efficiency. These results suggest that the adsorption of dye on M-G-CFP is controlled by the monolayer chemisorption reaction. This promising and unique hybrid structured material with high efficiency towards dye adsorption is attractive for wastewater treatment in industrial applications.

Conflicts of interest

There are no conflicts to declare.

Acknowledgements

The authors acknowledge financial assistance from the Department of Science and Technology (DST), Government of India, Grant # DST/INSPIRE/04/2014/015132.

References

1 S. Khan and A. Malik, *Environ. Sci. Pollut. Res.*, 2018, **25**, 4446–4458.
2 M. Vrijheid, M. Casas, M. Gascon, D. Valvi and M. Nieuwenhuijsen, *Int. J. Hyg. Environ. Health*, 2016, **219**, 331–342.
3 A. Ahmad, S. H. Mohd-Setapar, C. S. Chuong, A. Khatoon, W. A. Wani, R. Kumar and M. Rafatullah, *RSC Adv.*, 2015, **5**, 30801–30818.
4 D. Rajkumar and J. G. Kim, *J. Hazard. Mater.*, 2006, **136**, 203–212.
5 M. Oveisi, M. A. Asli and N. M. Mahmoodi, *J. Hazard. Mater.*, 2018, **347**, 123–140.
6 R. Gong, J. Ye, W. Dai, X. Yan, J. Hu, X. Hu, S. Li and H. Huang, *Ind. Eng. Chem. Res.*, 2013, **52**, 14297–14303.
7 A. Gil, F. C. C. Assis, S. Albeniz and S. A. Korili, *Chem. Eng. J.*, 2011, **168**, 1032–1040.
8 Y. Jin, J. Wu, J. Wang, Y. Fan, S. Zhang, N. Ma and W. Dai, *Inorg. Chim. Acta*, 2020, **503**, 119412.
9 Q. Liu, Y. Gao, Y. Zhou, N. Tian, G. Liang, N. Ma and W. Dai, *J. Chem. Eng. Data*, 2019, **64**, 3323–3330.
10 Z. Geng, Y. Lin, X. Yu, Q. Shen, L. Ma, Z. Li, N. Pan and X. Wang, *J. Mater. Chem.*, 2012, **22**, 3527.
11 B. Han and Y. H. Hu, *Energy Sci. Eng.*, 2016, **4**, 285–304.
12 M. Wu, L. Li, N. Liu, D. J. Wang, Y. C. Xue and L. Tang, *Process Saf. Environ. Prot.*, 2018, **118**, 40–58.
13 F. F. Jia, Q. M. Wang, J. S. Wu, Y. M. Li and S. X. Song, *ACS Sustainable Chem. Eng.*, 2017, **5**, 7410–7419.
14 X. Wang, J. Ding, S. Yao, X. Wu, Q. Feng, Z. Wang and B. Geng, *J. Mater. Chem. A*, 2014, **2**, 15958.
15 X. Q. Qiao, F. C. Hu, D. F. Hou and D. S. Li, *Mater. Lett.*, 2016, **169**, 241–245.
16 T. Liu, Y. Li, Q. Du, J. Sun, Y. Jiao, G. Yang, Z. Wang, Y. Xia, W. Zhang, K. Wang, H. Zhu and D. Wu, *Colloids Surf., B*, 2012, **90**, 197–203.
17 Y. Yuan, B. Liu, Q. Li, P. Shen and G. Chen, *J. Alloys Compd.*, 2017, **700**, 12–17.
18 X. Xu, J. Hu, Z. Yin and C. Xu, *ACS Appl. Mater. Interfaces*, 2014, **6**, 5983–5987.
19 S. Zhao, S. Xie, P. Sun, Z. Zhao, L. Li, X. Shao, X. Liu and Z. Xin, *RSC Adv.*, 2018, **8**, 17813–17825.
20 G. P. Awasthi, S. P. Adhikari, S. Ko, H. J. Kim, C. H. Park and C. S. Kim, *J. Alloys Compd.*, 2016, **682**, 208–215.
21 R. Sha, A. Gopalakrishnan, K. V. Sreenivasulu, V. V. S. S. Srikanth and S. Badhulika, *J. Alloys Compd.*, 2019, **794**, 26–34.
22 M. Thommes, K. Kanelo, A. V. Neimark, J. P. Olivier, F. R. Reinoso, J. Rouquerol and K. S. W. Sing, *Pure Appl. Chem.*, 2015, **87**, 1051–1069.
23 S. Kumar, V. Sharma, K. Bhattacharyya and V. Krishnan, *New J. Chem.*, 2016, **40**, 5185.
24 X. Zhuang, Y. Wan, C. M. Feng, Y. Shen and D. Y. Zhao, *Chem. Mater.*, 2009, **21**, 706–716.

25 T. Maneerung, J. Liew, Y. J. Dai, S. Kawi, C. Chong and C. H. Wang, *Bioresour. Technol.*, 2016, **200**, 350–359.
26 I. A. W. Tan, B. H. Hameed and A. L. Ahmad, *Chem. Eng. J.*, 2007, **127**, 111–119.
27 I. Langmuir, *J. Am. Chem. Soc.*, 1918, **40**, 1361.
28 H. M. F. Freundlich, *J. Phys. Chem.*, 1906, **57**, 385.
29 S. Han, K. Liu, L. Hu, F. Teng, P. Yu and Y. Zhu, *Sci. Rep.*, 2017, **7**, 43599.
30 P. Sharma, N. Hussain, D. J. Borah and M. R. Das, *J. Chem. Eng. Data*, 2013, **58**, 3477–3488.
31 S. Han, K. Liu, L. Hu, F. Teng, P. Yu and Y. Zhu, *Sci. Rep.*, 2017, **7**, 43599.
32 Q. Huang, M. Liu, J. Chen, Q. Wan, J. Tian, L. Huang, R. Jiang, Y. Wen, X. Zhang and Y. Wei, *Appl. Surf. Sci.*, 2017, **419**, 35–44.
33 H. Lu, J. Wang, B. Tian, X. Huang, J. Bi, T. Wang and H. Hao, *Chem. Eng. Technol.*, 2018, **41**, 1180–1187.
34 A. T. Massey, R. Gusain, S. Kumari and O. P. Khatri, *Ind. Eng. Chem. Res.*, 2016, **55**, 7124–7131.
35 Y. Fang, Q. Huang, P. Liu, J. Shi and G. Xu, *Colloids Surf., A*, 2018, **540**, 112–122.
36 H. J. Song, S. S. You and X. H. Jia, *J. Mater. Sci.: Mater. Electron.*, 2016, **27**, 10841–10848.
37 H. J. Song, S. You, X. H. Jia and J. Yang, *Ceram. Int.*, 2015, **41**, 13896–13902.
38 L. Chen, Y. Li, S. Hu, J. Sun, Q. Du, X. Yang, Q. Ji, Z. Wang, D. Wang and Y. Xia, *J. Exp. Nanosci.*, 2016, **11**, 1156–1170.
39 Y. Wu, M. Su, J. Chen, Z. Xu, J. Tang, X. Chang and D. Chen, *Dyes Pigm.*, 2019, **170**, 107591.

